Research Article

Influence of nanoflower $FeTiO_3$ in carbon dioxide reduction

Siva Palanisamy[1] · Surendhiran Srinivasan[1] · Arunkumar Prabhakaran Shyma[1] · Naveenkumar Rajendhran[1] · Karthik Subramani[1] · Vinoth Murugan[1] · Rajendran Venkatachalam[1,2]

Abstract

The effect of electrochemical reduction of carbon dioxide (CO_2) by changing the structure and morphology of $FeTiO_3$ nanoparticle prepared through sol–gel and hydrothermal methods is explained in this study. $FeTiO_3$ nanoparticles were used as a cathode where as a stainless steel plate and CO_2^- saturated $NaHCO_3$ were used as an anode and an electrolyte, respectively. The cyclic voltammetry and linear sweep voltammetry analysis were carried out comprehensively on $FeTiO_3$-SG-and $FeTiO_3$-HT-coated electrodes to decouple the electrochemical reduction processes of CO_2 in aqueous solution. The charge transfer resistance and the product gases were studied using electrochemical impedance spectroscopy and gas chromatography, respectively. The observed results were analyzed in light of structure/morphology, particle size, and surface area of $FeTiO_3$ nanoparticles and their influence on the effective cathodic behavior in CO_2 to CO reduction.

Keywords Electrochemical reduction · Nanoflower $FeTiO_3$ · Cyclic voltammetry · CO_2 reduction · Cathodic behavior

1 Introduction

The knowledge on the environmental impact of the greenhouse gas emission is mandatory to for health and environment. Even though, many processes are responsible for emission of the greenhouse gases, the CO_2 reduction and conversion by natural process need intensive studies [1–4]. The increased release of CO_2 to the environment as a result of emission of gases from natural/automotive/industries leads to its drastic increase in the atmosphere [5, 6]. This may lead to many adverse effects on the atmospheric and climatic conditions, resulting in global warming. To overcome these issues, it is essential to retain the desired CO_2 level in the atmosphere. An important way to address this issue is to capture, store, and reduce/convert the CO_2 from the atmosphere. Of several methods used for the reduction of CO_2, one method is the electrochemical method [4–9].

Electrocatalytic approaches of CO_2 conversion have gained attention because of their advantages: namely control of electrode potentials and reaction temperature, recycling of opinionated electrolytes to minimize its consumption as simple water or waste water, self-generation of electricity to drive the process without generating any new CO_2 sources, and a compact, modular, on-demand, and easy to scale up electronic system for CO_2 reduction [10]. Recently, electrochemical reductions of CO_2 on mercury and amalgam cathodes are used to produce formic acid [11–16]. Among the various metal oxides used for the cathodic reduction, the materials such as $FeTiO_3$ are used for simultaneous reduction of CO_2 and NO_2 [17]. Attempts are made to address the earth's greenhouse effect problem with TiO_2 as material for CO_2 electrochemical reduction in aqueous and non-aqueous media [18, 19].

To achieve it, RuO_2 and Pt co-supported on colloidal TiO_2 particles as redox catalyst in the presence of $Ru(bpy)_3^{2+}$ sensitizer are used in water photolysis to enhance the efficiency of water cleavages by visible light [20, 21].

Many Fe-based materials highly influence of the electrochemical performance, because the direct excitation

✉ Rajendran Venkatachalam, veerajendran@gmail.com | [1]Centre for Nano Science and Technology, K.S. Rangasamy College of Technology, Tiruchengode, Tamil Nadu 637 215, India. [2]Centre for Nanoscience and Technology, Dr. N. G. P. Arts and Science College, Dr. N. G. P. Kalapatti Road, Coimbatore, Tamil Nadu 641048, India.

SN Applied Sciences (2019) 1:1230 | https://doi.org/10.1007/s42452-019-1275-9

Received: 6 August 2019 / Accepted: 12 September 2019 / Published online: 17 September 2019

of the Fe–O in these with containing materials induces the electron transfer from O^{2-} to Fe^{3+} to form Fe^{2+}, which is responsible for the catalytic CO_2 reduction [22]. At different electrochemical system and condition Fe-based materials play very well like, Fe-containing MoF and TiO_3 showed photocatalytic for CO_2 reduction under visible light irradiation [22–24]. A flower like $FeTiO_3$ pronounced and stable pesudocapacitance has been found [25]. A careful review of literature indicates that conversion of CO_2 into liquid fuel is one of the most important contemporary energy storage and environmental challenges.

In this article, light of electrochemical reduction of carbon dioxide (CO_2) by changing the structure/morphology, particle size, and surface area of $FeTiO_3$ nanoparticles using sol–gel and hydrothermal methods. The prepared $FeTiO_3$-SG and $FeTiO_3$-HT nanoparticles were comprehensively characterized through different techniques such as X-ray diffraction (XRD), Brunauer–Emmett–Teller (BET), particle size distribution (PSD), Fourier transform infrared spectroscopy (FTIR), scanning electron microscope (SEM), transmission electron microscopy (TEM), electrochemical impedance spectroscopy (EIS), and gas chromatography (GC). The effective reduction of CO_2 into CO was carried out using nano-$FeTiO_3$ electrodes as a cathode material. The efficiency of electrocatalytic reduction of nano-$FeTiO_3$ electrodes obtained through both methods was explored based on the cyclic voltammetry (CV), impedance, and linear sweep voltammetry (LSV) test results.

2 Materials and methods

2.1 Materials

All the chemicals used in this investigation were AR grade procured from Merck, India, and were used without any further purification. The double-distilled (DD) water purified through Milli-Q (6110F; Ultrapure Water System, Germany; pH6.99) was used in this study to prepare all solutions.

2.2 Preparation of $FeTiO_3$ nanoparticles

The $FeTiO_3$ nanoparticles were prepared using two methods, namely sol–gel and hydrothermal methods, as detailed below:

Sol–gel Iron nitrate and ethanol were used as starting materials. First, 6.64 g iron nitrate was dissolved in 5 mL DD water. Then, 7 mL titanium butoxide was placed in a three-necked round flask and mixed with 10 mL ethanol to form a homogeneous solution. The iron nitrate solution was added drop-wise to the final solution. This reaction mixture was strongly stirred for 3 h. After the hydrolysis step, the fresh gel was dried at 100 °C for 24 h. Finally, the resulting dried powder was calcined at 700 °C for 10 h. The obtained powders, i.e., nano-$FeTiO_3$ (hereafter termed as $FeTiO_3$-SG) was used for further studies and coating on a stainless steel (SS) plate.

Hydrothermal method The first precursor solution was prepared by dissolving 1 M iron nitrate (2.41 g) in 10 ml DD water. The second precursor solution, that is, 0.5 M titanium isopropoxide was dissolved in 50 mL ethanol results in titanium tetraisopropoxide solution; 5 mL this solution was taken and then added to 10 mL iron nitride solution (the first precursor). The pH of the solution was adjusted above 10 by adding 3 M NaOH. The above solution was following the milled hydrothermal treatment. The solution was placed into

50 mL hydrothermal and heat-treated at 130 °C in the presence of magnetic string (800 rpm) for 3 h. The obtained precipitates were centrifuged several times. The obtained precipitates were dried in a vacuum oven at 100 °C for 12 h to remove the adsorbed water. Then, the dried precipitates were ground and the nano-$FeTiO_3$ powder (hereafter termed as $FeTiO_3$-HT) was used for further studies and coating on the SS plate.

2.3 Preparation of $FeTiO_3$ electrodes

The nano-$FeTiO_3$ electrode was prepared using doctor blade technique [26]. The SS plate from the SS304 grade and then cleaned using acetone. The synthesized $FeTiO_3$-SG powder and polyvinylidene fluoride were mixed at a ratio of 85:15. The mixture was added into a small quantity of *N*-methyl 2-pyroledine as a solvent to prepare the paste. The prepared $FeTiO_3$-SG was coated over the SS plate using doctor blade technique. After coating, $FeTiO_3$-SG electrode was dried in a hot-air oven at 85 °C for 1 h and then used for further studies. Using a similar procedure, $FeTiO_3$-HT was coated on the SS plate to obtain the $FeTiO_3$-HT electrode.

2.4 Electrocatalytic reduction of carbon dioxide

The electrocatalysis was carried out using a Terylene diaphragm cell with a capacity of 100 mL.A 4 × 4 cm SS304 grade plate was used as an anode where as $FeTiO_3$-SG-coated SS304 plate was used as a cathode. The anode and cathode were separated at a distance of 2 cm. A Teflon film was introduced in between the electrodes as a separator. The necessary electric potential was applied between the anode and cathode. The current/voltage flowing through the circuit was monitored through a dc monitor. The electrolyte used for this study was 1 M $NaHCO_3$. Before starting the experiment, the electrolyte was deoxygenated with nitrogen gas for 30 min. Then, CO_2

gas was passed into the setup for 30 min. The constant electrical potential (4 V) was applied across anode and cathode for 10 min. As a result of electrolysis, the reduction of the applied CO_2 gas took place and hence led to CO and its bi-products, as given below:

$$CO_{2(g)} \rightarrow CO_{2(ad)} \quad (1)$$

$$CO_{2(ad)} + e^- \rightarrow \cdot CO_2^- \quad (2)$$

$$\cdot CO_2^- + 2H^+ + e^- \rightarrow CO_{(precursor)} + H_2O \quad (3)$$

$$CO_{(precursor)} \rightarrow CO_{(g)} \quad (4)$$

The current flowing through the circuit during the nano-$FeTiO_3$ electrocatalysis was measured as 10.5–11.5 $mAcm^{-2}$. Using a similar procedure, with the same experimental setup, the electrocatalytic reduction with $FeTiO_3$-HT-coated electrode was carried out.

2.5 Characterization

The phase and crystalline nature of the synthesized samples were analyzed by an X-ray diffractometer (X'Pert PRO; PANalytical, the Netherlands) using Cu-Kα ($\lambda = 1.5406$ Å) as the radiation source. The samples were analyzed over the 2θ range, that is, 10°–80°at room temperature (298 K). The surface and subsurface morphology of nano-$FeTiO_3$ was viewed through an SEM (JSM-6390LV; JEOL, Japan) at 20 kV with a magnification of ×10,000 at 1 µm scale. The TEM images were obtained using a Gatan Quantum ER 965 Imaging filter installed on the instrument (TEM; JEOL). The observed images revealed information about the surface of the sample. The functional groups present on the prepared nano-$FeTiO_3$ were analyzed using FTIR (Spectrum 100; Spectrum 100; Perkin Elmer, USA). The spectra were recorded in the range between 4000 and 400 cm^{-1}.

After the CO_2 reduction, the obtained gas products were analyzed using GC (GC-QP2010 Ultra column, Rt-Q-BOND + Guard column; Shimadzu, Japan).At atmospheric pressure, after N_2 was purged, the CO_2 was continuously purged through a cell at 5 ml min^{-1} for 30 min to saturate the electrolyte. A constant potential was applied for 10 min for the electrocatalytic reduction, as discussed previously. The effluent sample was analyzed via the GC column [30 mL × 0.32 mmL.D, 10 µm + Guard column (3 mL × 0.32 mmL.D)].

The specific surface area of the obtained nano-$FeTiO_3$ was calculated using the BET method with a BET surface area analyzer (Autosorb AS-1MP; Quantachrome, USA). The samples were degassed under vacuum at 295 °C for 3 h to remove the physisorbed moisture. The physisorption analysis was carried out with N_2 adsorption–desorption measurements ata liquid nitrogen temperature (– 196 °C). Very low temperature was used to avoid any thermally induced changes on the surface of the particles. The PSD of $FeTiO_3$ nanoparticles was determined by a particle size analyzer (Nanophox; Sympatec, Germany) based on the dynamic light scattering technique.

2.6 Electrochemical measurements

The electrocatalysis study was carried out using the terylene diaphragm cell setup with a capacity of 100 mL. Then, 1 M $NaHCO_3$ was added to the setup followed by passing N_2 gas for 30 min. Following deoxidation, the three-cell setup was constructed inside the terylene diaphragm. Nano-$FeTiO_3$-coated SS304 plate, platinum mesh, and saturated calomel were used as a working electrode, counter electrode, and reference electrode, respectively.

The electrodes were placed in a triangular manner by keeping 1 cm distance between them. After 5 min, CV and LSV tests were carried out for both $FeTiO_3$-SG-and $FeTiO_3$-HT-coated electrodes by passing an electrical potential in the range from – 1 to 1 V at 10 mV s^{-1}. The same electrode configuration and electrolyte preparation were used for electrochemical measurements. After the construction of cell setup, CO_2 gas was passed through the system for 30 min. After purging the CO_2 gas, the CV and LSV results were obtained for both $FeTiO_3$-SG and $FeTiO_3$-HT-coated electrodes in the potential range from – 1 to 1 V at 10 mV s^{-1}.

The EIS study was carried out to explore the charge transfer process between working electrodes and solution interfaces. An electric potential between 1.2 and 0.1 V was applied at amplitude of 100 mV over the frequency range from 0.01 Hz to 1 MHz to carry out EIS studies for $FeTiO_3$-SG and $FeTiO_3$-HT-coated electrodes. The potential was applied after the stabilization of open current voltage. All electrochemical studies were carried out using Autolab (PGSTAT302 N; Metrohm Autolab, the Netherlands) at room temperature.

3 Results and discussion

3.1 X-ray diffraction

The XRD patterns for $FeTiO_3$-SG and $FeTiO_3$-HT nanoparticles are shown in Fig. 1. In the XRD pattern of $FeTiO_3$-SG, the set of reflections observed at $2\theta = 23.97°$, 32.16°, 39°, 49.32°, 53.76°, and 64.2° corresponding to the planes (012), (104), (006), (024), (116), and (300) confirm the $FeTiO_3$ rhombohedral structure (JCPDS file no.75-1211). Similarly, the XRD pattern for $FeTiO_3$-HT in Fig. 1b shows a set of reflections from ilmenite $FeTiO_3$ at the diffraction angle peaks at $2\theta = 23.97°$, 32.04°, 35.66°, 39°, 40.32°, 49.32°,

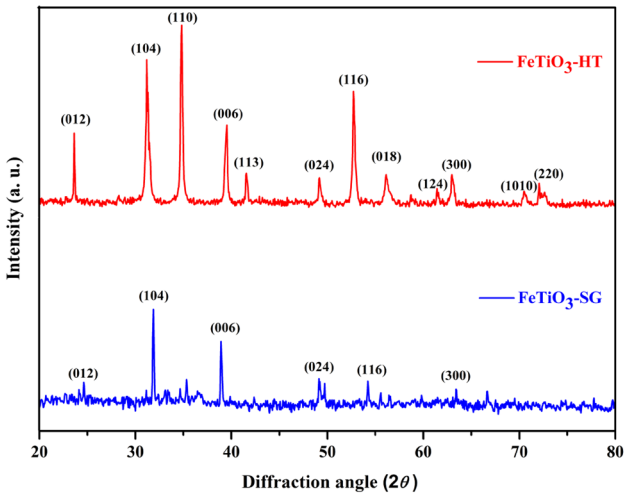

Fig. 1 X-ray diffraction pattern of nano $FeTiO_3$ particles

53.76°, 57 09°, 62.36°, 64.20°, 72°, and 74.5°corresponding to the planes (012), (109), (110), (006), (113), (024), (116), (018), (124), (300), (1010), and (220) once again reveal the rhombohedral structure of $FeTiO_3$ (JCPDS file no. 01-075-1211). Further, the XRD patterns clearly demonstrate that $FeTiO_3$-HT is more crystalline than $FeTiO_3$-SG.

Figure 2 represents for XRD patterns of $FeTiO_3$-SG and $FeTiO_3$-HT nanoparticles coated electrodes obtained after the electrochemical process. In both XRD patterns, all the characteristic peaks for $FeTiO_3$ nanoparticleswere observed and also some unidentified peaks were raised due to the chemical process occurs between $FeTiO_3$ nanoparticles coated electrodes and $NaHCO_3$ electrolyte during the electrochemical studies. After the electrochemical process, there is very small change in peak angle and intensity. Peaks were shifted towards lower angle and intensities were decreased for some peaks. During the electrochemical process, Na^+ ions were passivation on surface of the electrode so that only aforesaid changes i.e., peak angle and intensity were identified.

3.2 SEM and TEM

The SEM and TEM images of $FeTiO_3$-SGand $FeTiO_3$-HT are shown in Figs. 3 and 5, respectively. The surface morphology of $FeTiO_3$-SG nanoparticles (Fig. 3) reveals nonuniform shape of particles with size 200 nm.

However, smooth surfaces nanoflower-like morphology with a different scan rate was noticed in $FeTiO_3$-HT nanoparticles (Fig. 4). The observed TEM image for $FeTiO_3$-HT nanoparticles (Fig. 5b) reveals a typical nanoplate of nanoflowers with limited aggregation than that for $FeTiO_3$-SG nanoparticles (Fig. 5a).

3.3 The PSD and BET

The measured surface area and particle size of $FeTiO_3$-SG and $FeTiO_3$-HT nanoparticles are shown in Figs. 6 and 7, respectively. The average particle size measured through PSD technique for both $FeTiO_3$-SGand $FeTiO_3$-HT nanoparticles is 50 and 34 nm, respectively. The BET surface area for $FeTiO_3$-HT nanoparticles is large (197.1 m^2g^{-1}) compared to that for $FeTiO_3$-SG nanoparticles (178.5 m^2g^{-1}) (Table 1).

The observed approximately 10% increase in the BET surface area of $FeTiO_3$-HT nanoparticles is due to decrease in particle size (i.e., more than 45%) of nanoparticle prepared through hydrothermal method. The observed

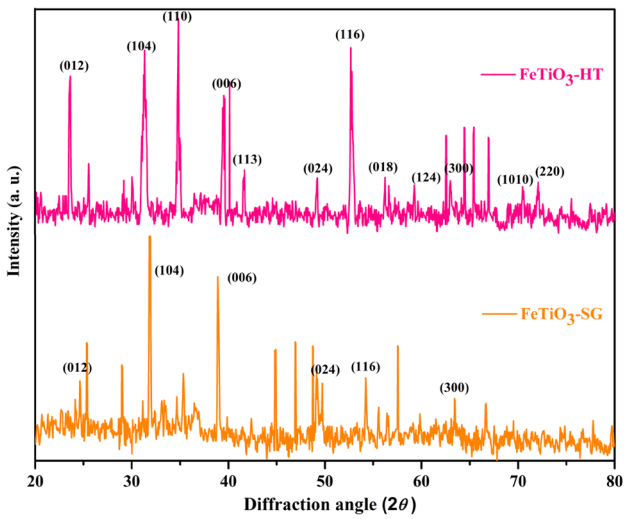

Fig. 2 After electrochemical reaction X-ray diffraction pattern of nano $FeTiO_3$ particles

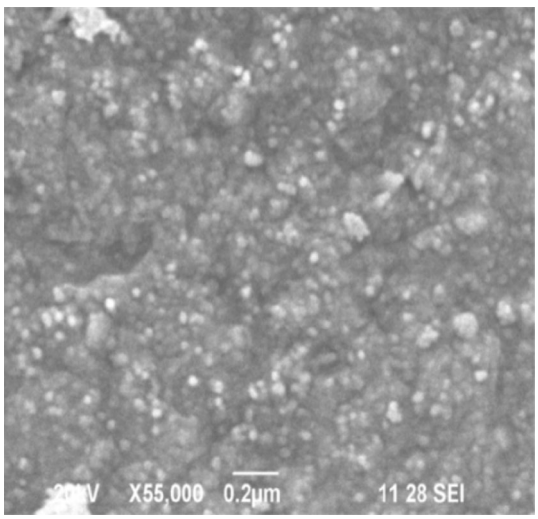

Fig. 3 Scanning electron microscope images of nano $FeTiO_3$-SG particles

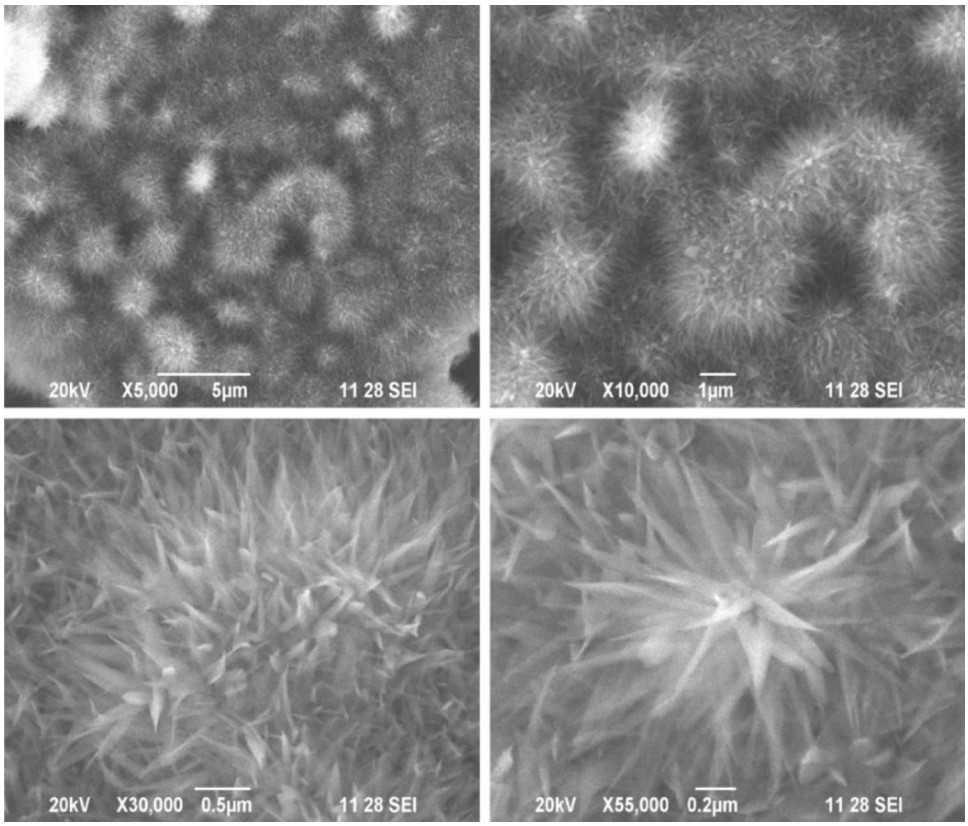

Fig. 4 Scanning electron microscope images of nano $FeTiO_3$-HT particles at four different scan rate

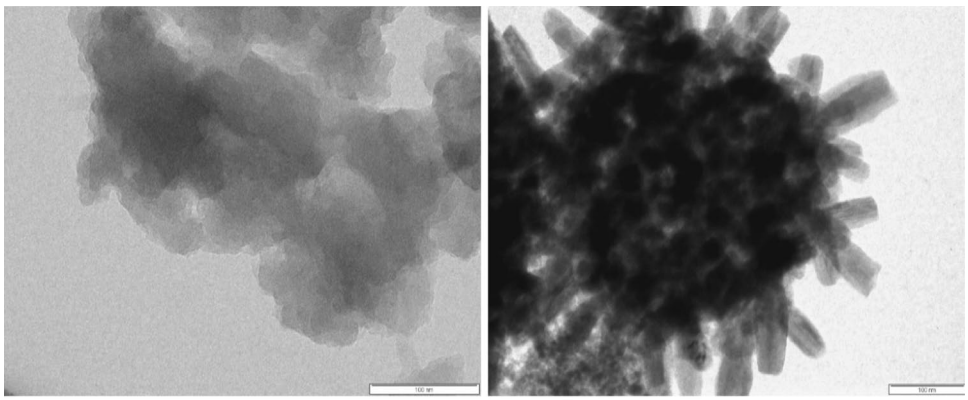

(a) $FeTiO_3$-SG **(b)** $FeTiO_3$-HT

Fig. 5 Transmission electron microscope images nano $FeTiO_3$ particles

results from the BET and PSD measurements show lower particle size with high surface area for $FeTiO_3$ nanoflower structure obtained through hydrothermal method. In addition, the above study also supports the observation made through SEM and TEM studies.

3.4 FTIR spectra

The FTIR spectra for the $FeTiO_3$-SG-and $FeTiO_3$-HT-coated electrodes before and after electroreduction are shown in Fig. 8. The absence of any peak on nano-$FeTiO_3$-coated electrode before electroreduction (Fig. 8a) indicates absence of carboxylic peaks (–COOH). After reduction, the $FeTiO_3$-SG-coated electrode shows two characteristic infrared absorption peaks at 1640 and 1384 cm^{-1} (Fig. 8b). The observed stretching peak at 1640 cm^{-1} can be attributed to the presence of carboxyl groups [27]. These functional groups have a key role in deposition on the surface of the $FeTiO_3$-SG-coated electrode after reduction. The peaks at 1384 cm^{-1} originate from the O–H bending vibration of –COOH [28].

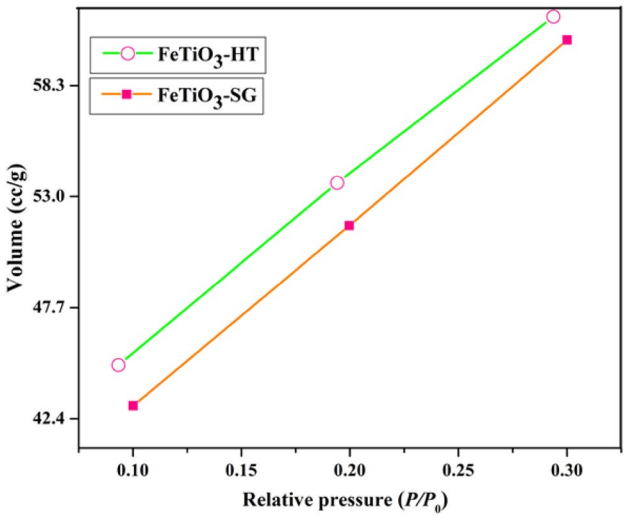

Fig. 6 Branauer-Emmett-Teller surface area of nano $FeTiO_3$ particles

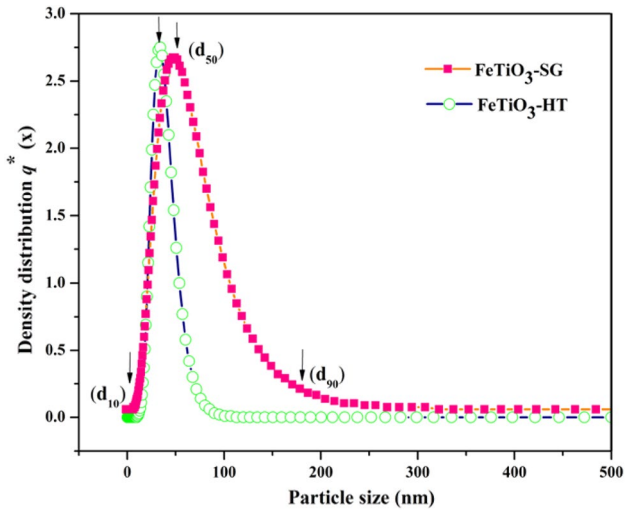

Fig. 7 The particle size distribution of nano $FeTiO_3$ particles

Table 1 Particle size and Branauer-Emmett-Teller surface area analysis for nano $FeTiO_3$ particles

Sample name	Particle size (nm)	BET surface area ($m^2\ g^{-1}$)
Nano $FeTiO_3$-SG	50	178.5
Nano $FeTiO_3$-HT	34	197.1

Similarly, after reduction, the $FeTiO_3$-HT-coated electrode shows two characteristic infrared absorption peaks at 1628 and 1327 cm^{-1} (Fig. 8d).The observed stretching peak at 1628 cm^{-1} is due to the presence of carboxyl groups [27], which is mainly responsible for the deposition on the surface of the $FeTiO_3$-HT-coated

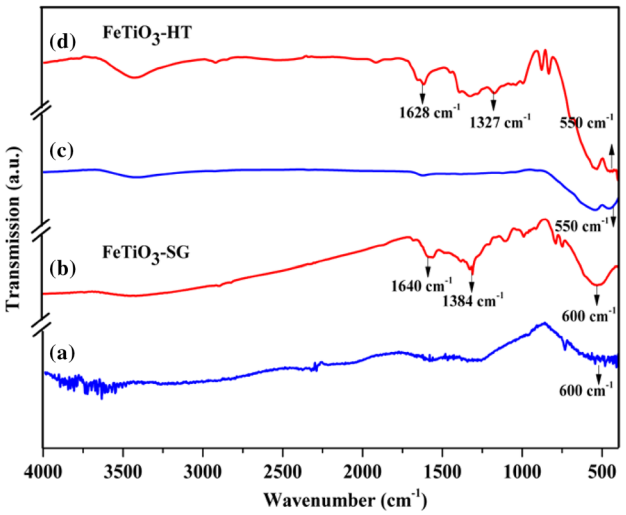

Fig. 8 Fourier transform infrared spectra of nano $FeTiO_3$ coated electrodes

electrode after reduction. The peak at 1327 cm^{-1} is due to HCO bending [29]. However, before reduction (Fig. 8c), the $FeTiO_3$-HT-coated electrode does not show any clear peaks as observed in the $FeTiO_3$-SG-coated electrode (Fig. 8a). Commonly, the bands observed in the low wave number region (400–650 cm^{-1}) can be assigned to Ti–O bond vibrations in the $FeTiO_3$-SG-and $FeTiO_3$-HT coated electrodes before and after reductions. Thus, the absorption bands of Ti–O octahedral appearing at 600 and 550 cm^{-1} correspond to the formation of $FeTiO_3$ [29].

3.5 Gas chromatography

The GC is generally used for separating different components from mixtures and to determine the relative amount of such components [30–32]. The catalytic activity of nano-$FeTiO_3$ toward CO_2 reduction is clearly visible from the obtained GC results. Figure 9 shows the product of CO formed after nano-$FeTiO_3$ assisted CO_2 reduction [33, 34]. While comparing the CO peaks, it is clear that the amount of CO generated is almost identical for both $FeTiO_3$-SG and $FeTiO_3$-HT.

3.6 Electrochemical impedance spectroscopy

A plot is drawn between the real part (Z′) and the imaginary part (Z″) of impedance, which is known as Nyquist plot. Impedance characteristics are measured between the ranges from 1 Hz to 1 MHz in 1 M $NaHCO_3$ electrolyte solution. Figure 10 shows the Nyquist plot representation for $FeTiO_3$-SG-and $FeTiO_3$-HT-coated electrodes. The obtained Nyquist plot was interpreted into an equivalent

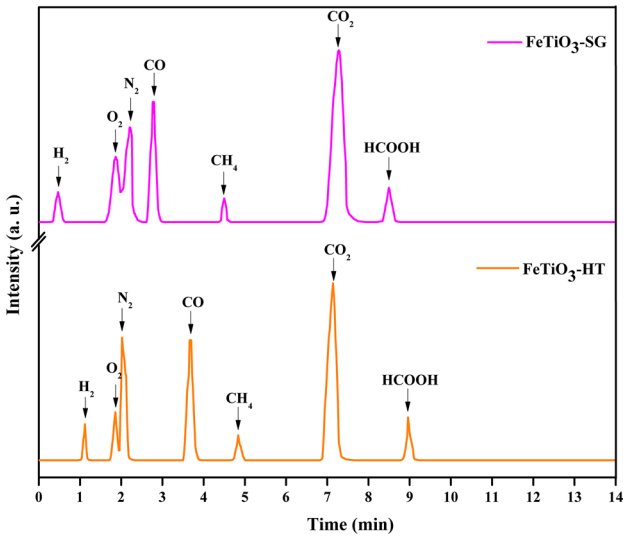

Fig. 9 Gas chromatogram of the gaseous products after CO_2 reduction

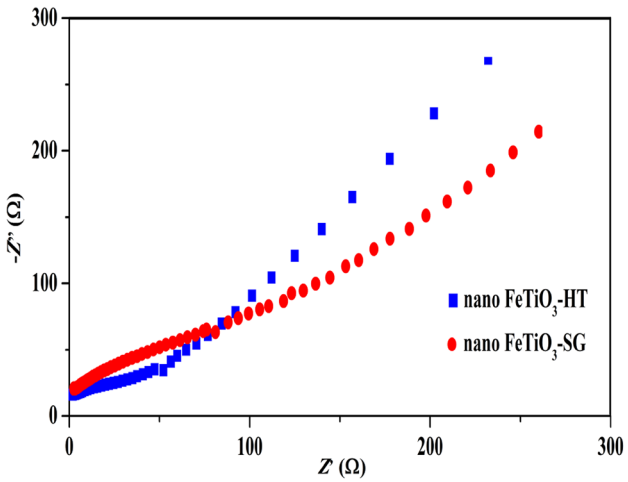

Fig. 10 Nyquist plots for nano FeTiO3 particles coated electrodes

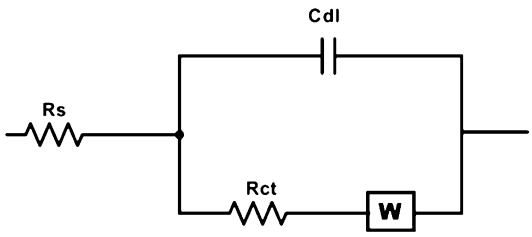

Fig. 11 Equivalent circuit model

circuit model (Fig. 11) representing with solution resistance (R_s), charge transfer resistance (R_{ct}), Warburg impedance (W) and constant phase element. This circuit model was applied to the ionic conductivity of the $FeTiO_3$-SG and $FeTiO_3$-HT was measured.

It can be observed that the synthesis method causes the difference in semicircle and small arc for both samples, meaning an effective electron–hole pairs. The Fig. 10 presented is used to illustrate the relative and the change of impedance depends on processing parameters, it is clearly observed that the $FeTiO_3$-SG coated electrode exhibit semi parabolic arc at higher potential and have high impedance. When looking for $FeTiO_3$-HT coated electrode, shows the smallest semi parabolic arc at lower potential, it representing the smallest charge transfer resistance and the highest conductivity efficiency of the same electrode. The lower charge transfer resistance leads to lower total internal resistance, which is better for higher ionic conductivity [35]. From the obtained results, comparison between both electrodes, the low angle Warburg impedance relative to the control indicating that the $FeTiO_3$-HT coated electrodes have efficient movement of electrons and low resistance. This suggests that the $FeTiO_3$-HT coated electrode have higher ionic conductivity compared with $FeTiO_3$-SG electrode.

Since the electrical and ionic conductivity varied with the surface morphologies, surface area and average particle size distributions. The porous nature of the material is depends upon the materials morphology. Because pore present in sample is very important parameter towards electrode electrolyte interaction and charge transfer process, the ionic conductivity of materials increases with the decrease of average particle size distributions [36].

The $FeTiO_3$-HT sample have high surface area (197.1 $m^2\ g^{-1}$), low average particle size (39 nm), and also with nanoflower-like structure lead to higher ionic conductivity and low resistance compared with $FeTiO_3$-SG which was prepared by sol–gel method, obtained with higher particle size (50 nm) and low surface area (178.5 $m^2\ g^{-1}$) with nonuniformly (agglomerated). A similar observation by electrochemical impedance spectra studies on gold nanoparticles for CO_2 reduction is reported elsewhere [33, 34].

3.7 Cyclic voltammetry

The choice of a suitable electrolyte for studying CO_2 reduction in the $FeTiO_3$-SG-and $FeTiO_3$-HT-coated electrodes is quite a complex question because of the known tendency of a number of ions to absorb irreversibly on the surface of $FeTiO_3$. The CV analysis carried out on the SS plate and $FeTiO_3$-SG-and $FeTiO_3$-HT-coated electrodes is shown in Fig. 12. The electrochemical behaviors of the prepared electrolytes were examined using mercury electrode as the reference electrode and Pt wire as the counter electrode. Figure 12a–f reveal the CV for the SS

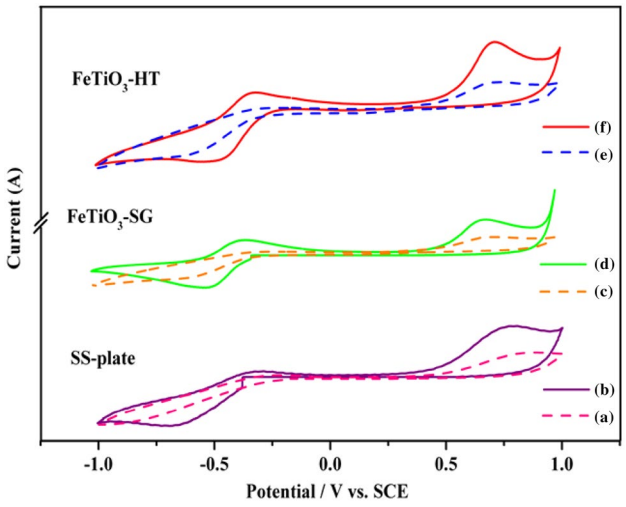

Fig. 12 Cyclic Voltammetry of SS plate, nano $FeTiO_3$-SG and $FeTiO_3$–HT particles coated electrodes of only N_2 and both N_2 with CO_2 saturated in 1 M $NaHCO_3$ at 10 mVs^{-1}. (a) SS plate-only N_2, (b) SS plate-N_2 with CO_2, (c) nano $FeTiO_3$-CP-only N_2, (d) nano $FeTiO_3$-CP-N_2 with CO_2, (e) nano $FeTiO_3$-MW-only N_2, (f) nano $FeTiO_3$-MW-N_2 with CO_2

plate, $FeTiO_3$-SG-coated electrode and $FeTiO_3$-HT-coated electrode with N_2-saturated 1 M $NaHCO_3$ and N_2; CO_2^- saturated 1 M $NaHCO_3$ at 10 mVs^{-1} scan rate at room temperature.

The CV for the SS plate, $FeTiO_3$-SG-coated electrode, and $FeTiO_3$-HT-coated electrode after passing N_2 gas into the electrolyte is shown in Fig. 12a, c, e. The absence of reduction peaks in the sweeping region from − 1 to 1 V is observed in both samples. Figure 12b, d, f reveal the CV for the SS plate, $FeTiO_3$-SG-coated electrode, and $FeTiO_3$-HT-coated electrode with CO_2-saturated 1 M $NaHCO_3$.

The observed clear reduction peaks in both samples between − 0.4 and − 0.2 V are perhaps due to the one-electron reduction of CO_2, which in turn generates an anion radical of CO_2, resulting in the reduction of CO_2 to CO_2^- [37]. This anion radical, however, reacts rapidly with the intermediate of the desired product, already discussed in GC. Figure 12d, f show shifting of the reduction peaks toward the positive side, that is, from − 0.4 to − 0.2 V. Hence, a sharp increase in the cathode current and the cathodic behavior is described due to $FeTiO_3$ nanoparticles than $FeTiO_3$-SG and SS plate. The above CV results indicate a more favorable effect on Fe-doped TiO_2 while increasing the cathodic reduction (from − 0.4 to − 0.2 V) for the electrochemical species Ag^--, Pt^--, and Ru^--doped TiO_2, as reported earlier [38, 39]. The above study confirms that the $FeTiO_3$ nanoparticle-modified electrodes can be an ideal material for electrocatalytic activity reduction of CO_2. The flowerlike morphology is expected to provide a larger electrode–electrolyte contact area, good diffusion of electrolyte right through the electrode, and a suitable conduction pathway for electrons traveling in the active component of the electrode [25].

Figure 13a, b reports the voltammetric profiles obtained for the $FeTiO_3$ based electrodes at different loading [40, 41]. An oxidation–reduction contribution is observed between − 1 V and 1 V, which depends on the catalytic loading. However, the main characteristic of the Voltammogram is a reduction process, starting at around − 0.2 V.

3.8 Linear sweep voltammetry

The LSV tests for the electrochemical activity of CO_2 reduction for the $FeTiO_3$-SG-and $FeTiO_3$-HT-coated electrodes are shown in Fig. 14. The existence of the reduction of CO_2 in both $FeTiO_3$-SG-and $FeTiO_3$-HT-coated electrodes can be seen from Fig. 13a, b, respectively. A high reduction peak is observed at − 0.4 and − 0.2 V for $FeTiO_3$-SG-and $FeTiO_3$-HT-coated electrodes, respectively. This is

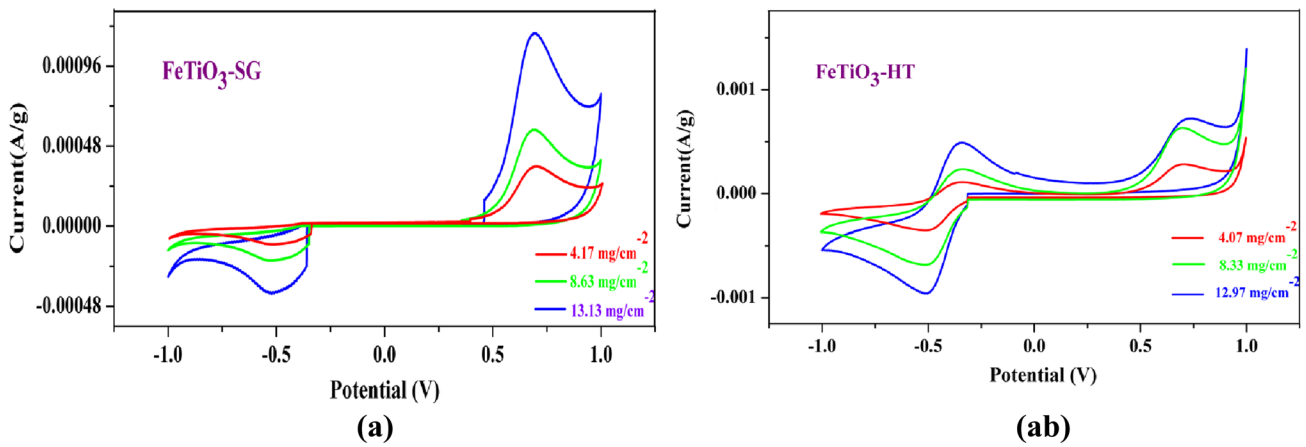

Fig. 13 Nano $FeTiO_3$-based electrodes at different loadings

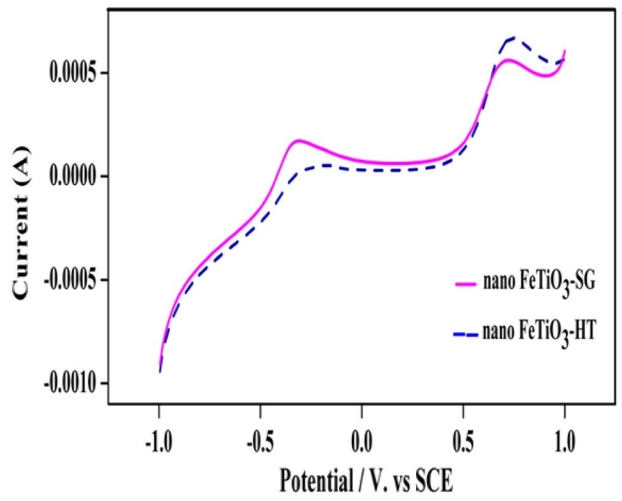

Fig. 14 Linear sweep voltammetry of nano $FeTiO_3$ particles coated electrodes in N2 and CO_2 saturated in 1 M $NaHCO_3$ at scan rate mVs^{-1}

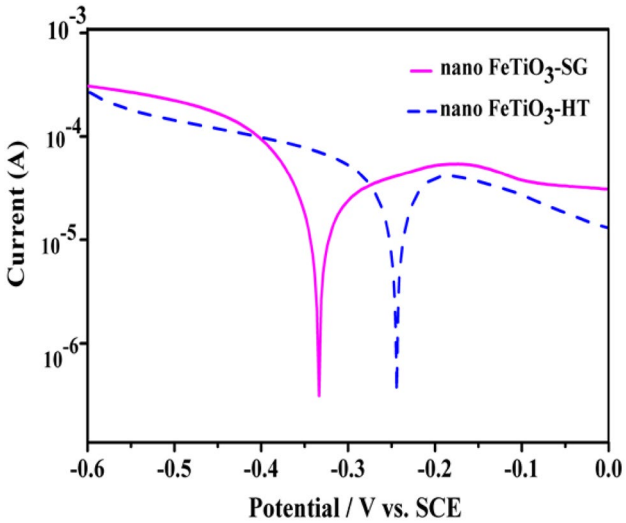

Fig. 15 Tafel plot for linear sweep voltammetry of nano $FeTiO_3$ particles coated electrodes in N_2 and CO_2 saturated in 1 M $NaHCO_3$ at scan rate 10 mV s^{-1}

again confirmed from the Tafel plots for $FeTiO_3$-SG-and $FeTiO_3$-HT-coated electrodes, as shown in Fig. 15. The Tafel plots confirm the reduction peak at − 0.3 and − 0.2 V for $FeTiO_3$-SG-and $FeTiO_3$-HT-coated electrodes, respectively.

Above results confirm that the $FeTiO_3$-HT nanoparticle-coated electrode show a slightly positive shift in the reduction peak compared to the $FeTiO_3$-SG-coated electrode. The observed high cathodic behavior of the $FeTiO_3$-HT-coated electrodes is due to the high surface area and nanoflower structure as evidenced from the observation made through XRD, SEM/TEM, and other studies. Nanoflower shows high surface to volume ratio to increase surface adsorption for accelerating the kinetics of reactions and it is future trend of multi application [25, 42–44].

4 Conclusion

The above studies confer that uniformly nanoflower-like structure and high surface area of $FeTiO_3$ nanoparticles prepared through hydrothermal method show a better cathodic behavior than nonuniformly structured low-surface-area $FeTiO_3$ nanoparticles prepared through sol–gel method for CO_2 to CO reduction. The FTIR spectra show the existence of absorbed functional carbonyl group in both $FeTiO_3$-SG and $FeTiO_3$-HT. After the electrochemical reduction, more sharp peaks were obtained on the $FeTiO_3$-HT-coated electrode surface than the $FeTiO_3$-SG-coated electrode. GC study confirms the reduction of $FeTiO_3$ to form CO form CO_2 and other hydrocarbons with low current density. The EIS studies confirm a low charge transfer resistance in case of $FeTiO_3$-HT-coated electrode. The studies indicate an enhancement in the cathodic reduction (− 0.4 to − 0.2 V) on the Fe-doped TiO_2 than the Ag^{-}-, Ro^{-}-, and Pt^{-}-doped TiO_2. The LSV studies further support the observation made on CV by showing the reduction peak at lower potential, that is, − 0.3 V in case of the nano-$FeTiO_3$-coated electrode where as it occurs slightly at higher potential, that is, − 0.2 V for the nano-$FeTiO_3$-coated electrode.

Compliance with ethical standards

Conflict of interest The authors declare that they have no conflict of interest.

References

1. Ivan M-G, Enrique A-G, Jonathan A, Angel I (2016) Electrochemical membrane reactors for the utilisation of carbon dioxide. Chem Eng J 305:104–120
2. Albo J, Alvarez-Guerra M, Castaño P, Irabien A (2015) Towards the electrochemical conversion of carbon dioxide into methanol. Green Chem 17:2304–2324
3. Merino-Garcia I, Albo J, Irabien A (2017) Tailoring gas phase CO_2 electroreduction selectivity to hydrocarbons at Cu nanoparticles. Nanotechnology 29(1):014001
4. Merino García I, Albo J, Irabien A (2017) Productivity and selectivity of gas phase CO_2 electroreduction to methane at Cu nanoparticle-based electrodes. Energy Technol 5(6):922–928
5. Jonathan A, Alfonso S, Jose S-G, Vicente M, Angel I (2015) Production of methanol from CO_2 electroreduction at Cu_2O andCu_2O/ZnO-based electrodes in aqueous solution. Appl Catal B 176:709–717

6. Jonathan A, Angel I (2016) Cu_2O-loaded gas diffusion electrodes for the continuous electrochemical reduction of CO_2 to methanol. J Catal 343:232–239
7. Jonathan A, Daniel V, Garikoitz B, Oscar C, Pedro C, Angel I (2017) Copper-based metal-organic porous materials for CO_2 electrocatalytic reduction to alcohols. Chemsuschem 10(6):1100–1109
8. Jonathan A, Garikoitz B, Pedro C, Angel I (2017) Methanol electrosynthesis from CO_2 at Cu_2O/ZnO prompted by pyridine-based aqueous solutions. J CO2 Util 18:164–172
9. Song Y, Peng R, Hensley DK, Bonneson PV, Liang L, Wu Z, Mayer HM, Chi M, Ma C, Sumpter BG, Rondinone AJ (2016) High-selectivity electrochemical conversion of CO_2 to ethanol using a copper nanoparticle/N-doped graphene electrode. Chem Sel 1:1–8
10. Jinli Q, Yuyu L, Feng H, Jiujin Z (2014) A review of catalysts for the electroreduction of carbon dioxide to produce low-carbon fuels. Chem Soc Rev 43:631–675
11. Fischer F (1912) Praktikum der elektrochemie. Springer, Berlin
12. Constentin C, Drouet S, Robert M, Savent JM (2012) A local proton source enhances CO_2 electroreduction to CO by a molecular Fe catalyst. Science 338:90–94
13. Back S, Yeom MS, Jung Y (2015) Active sites of Au and Ag nanoparticle catalysts for CO_2 electroreduction to CO. ACS Catal 5:5089–5096
14. Chen Y, Li CW, Kanan MW (2012) Aqueous CO2 reduction at very low over potential on oxide-derived Au nanoparticles. J Am Chem Soc 134:19969–19972
15. Varela AS, Kroschel M, Reier T, Strasser P (2016) Controlling the selectivity of CO_2 electroreduction on copper: the effect of the electrolyte concentration and the importance of the local pH. Catal Today 260:8–13
16. Kokoszka B, Jarrah NK, Liu C, Moore DT, Landskron K (2014) Supercapacitive swing adsorption of carbon dioxide. Chem Int Ed 53:3698–3701
17. Siva P, Prabhu P, Selvam M, Karthik S, Rajendran V (2017) Electrocatalytic conversion of carbon dioxide to urea on nano $FeTiO_3$ surface. Ionics 23(7):1871–1878
18. Tseng WC, Chang J, Wu CS (2002) Effects of sol–gel procedures on the photocatalysis of Cu/TiO_2 in CO_2 photoreduction. Appl Catal B Environ 37:37–48
19. Peebles DE, Goodman DW, White JM (1983) Methanation of carbon dioxide on nickel (100) and the effects of surface modifiers. J Phys Chem 87:4378–4387
20. Wang W, Wang S, Ma X, Gong J (2011) Recent advances in catalytic hydrogenation of carbon dioxide. Chem Soc Rev 40:3703–3727
21. Bordgarello E, Kiwi J, Pelizzetti E, Visca M, Gratzell M (1981) Photochemical cleavage of water by photocatalysis. Nature 289:158–160
22. Wang D, Huang R, Liu W, Sun D, Li Z (2014) Fe-based MOFs for photocatalytic CO_2 reduction: role of coordination unsaturated sites and dual excitation pathways. ACS Catal 4:4254–4260
23. Troung QD, Le TH, Liu JY, Chung CC, Ling YC (2012) Synthesis of TiO_2 nanoparticles using novel titanium oxalate complex towards visible light–driven photocatalytic reduction of CO_2 to CH_3OH. Appl Catal A 437:28–35
24. Ouaida MB, Badie JM, Flamant G (1985) High temperature thermochemical treatment of ilmenite $FeTiO_3$ in solar chemical reactors. Solar Wind Technol 2:15–24
25. Tao T, Glushenkov AM, Hongwei L, Zongwen L, Xiujuani JD, Hua C, Ringer SP, Ying C (2011) Ilmenite FeTiO3 nanoflowers and their ehavioracitance. J Phys Chem C 115(35):17297–17302
26. Selvam M, Saminathan K, Siva P, Saha P, Rajendran V (2016) Corrosion ehavior of Mg/graphene composite in aqueous electrolyte. Mater Chem Phys 172:129–136
27. Zhang YX, Dai L, Kong WX, Chen LW (2012) Characeterization and in vitro antioxidant activities of polysaccharides from Pleurotus ostreatus. Int J Biol Macromol 51:259–265
28. Fangfei L, Suqin L, Qiuju F, Shuxin Z, Jinbao Z, Peng B (2012) Electrochemical synthesis of dimethyl carbonate with carbon dioxide in 1-Butyl-3-methylimidazoliumtetrafluoborate on indium electrode. Int J Electrochem Sci 7:4381–4387
29. Ojamae L, Christian A, Henrik P, Käll PO (2006) IR and quantum-chemical studies of carboxylic acid and glycine adsorption on rutile TiO_2 nanoparticles. J Colloid Interface Sci 296:71–78
30. Shen J, Kortlever R, Kas R (2015) Electrocatalytic reduction of carbon dioxide tocarbon monoxide and methane at an immobilized cobalt protoporphyrin. Nat Commun 6:1–8
31. Huang LL, Hu HC, Chen LH (2015) Determination of total acid content in biomass hydrolysates by solvent-assisted and reaction based headspace gas chromatography. J Chromatogr A 1422:13–17
32. Hong J, Zhang W, Ren J, Xu R (2013) Photocatalytic reduction of CO_2: a brief review on product analysis and systematic methods. Anal Methods 5:1086–1097
33. Oh Y, Hu X (2015) Ionic liquids enhance the electrochemical CO_2 reduction catalyzed by MoO_2. Chem Commun 51:13698–13701
34. Liu M, Pang Y, Zhang B, Luna PD (2016) Enhanced electrocatalytic CO_2 reduction via field-induced reagent concentration. Nat Res Lett 537:382–386
35. Li W, Jishi Z, Xiangming H, Jian G, Jianjun L, Chunrong W, Changyin J (2011) Electrochemical impedance spectroscopy (EIS) study of $LiNi_{1/3}Co_{1/3}Mn_{1/3}O_2$ for Li-ion batteries. Int J Electrochem Sci 7:345–353
36. Seongkoo C, Chien-Fan C, Partha P-M (2015) Influence of microstructure on impedance response in intercalation electrodes. J Electrochem Soc 162(7):A1202–A1214
37. Hongzhou Y, Yanlong G, Youguan D, Feng S (2002) Electrochemical activation of carbon dioxide inionic liquid: synthesis of cyclic carbonates at mild reaction conditions. Chem Commun 3:274–275
38. Luisa FCG, Nora AGG, Hugo AM, Eduardo MS (2014) Electrochemical study of TiO_2 modified with silver nanoparticles upon CO_2 reduction. J Appl Electrochem 44:675–682
39. Milena K, Alania M, Jan A (1984) Electrocatalysis of the cathodic reduction of carbon dioxide on platinized titanium dioxide film electrodes. J Electrochem Soc 3:745–750
40. Albo J, Saez A, Solla-Gullon J, Montiel V, Irabien A (2015) production of methanolfrom CO_2 electroreduction at Cu2O and Cu2O/ZnO-based electrodes in aqueous solution. Appl catal B-environ 176:709–717
41. Siva P, Arunkumar PS, Surendhiran S, Rajendran V (2019) Novel modifed nano-activated carbon and its influence on the metal–O_2 battery system. J Energy Storage 22:283
42. Liu Y, Chen J, Du M (2017) The preparation of dual-functional hybrid nanoflower and its application in the ultrasensitive detection of disease-related biomarker. Biosens Bioelectron 92:68–73
43. Ma J, Ren W, Zhao J (2010) Growth of TiO_2 nanoflowers photoanode for dye-sensitized solar cells. Nano Lett 10:2562–2567
44. Lakkakula RJ, Matshaya T, Macedo RW (2017) Cationic cyclodextrin/alginate chitosan nanoflowers as 5-fluorouracil drug delivery system. Mater Sci Eng C Mater Biol Appl 70:169–177